IOP Publishing | Institute of Physics and Engineering in Medicine Physics in Medicine & Biology

Phys. Med. Biol. **62** (2017) 7784–7797 https://doi.org/10.1088/1361-6560/aa8945

Point spread function based image reconstruction in optical projection tomography

Anna K Trull[1], Jelle van der Horst[1], Willem Jan Palenstijn[2], Lucas J van Vliet[1], Tristan van Leeuwen[3] and Jeroen Kalkman[1]

[1] Department of Imaging Physics, Delft University of Technology, Lorentzweg 1, 2628 CJ Delft, Netherlands
[2] Computational Imaging, Centrum Wiskunde & Informatica, Science Park 123, 1098 XG Amsterdam, Netherlands
[3] Mathematical Institute, Utrecht University, Budapestlaan 6, 3584 CD Utrecht, Netherlands

E-mail: a.k.trull@tudelft.nl

Received 7 August 2017
Accepted for publication 30 August 2017
Published 20 September 2017

Abstract

As a result of the shallow depth of focus of the optical imaging system, the use of standard filtered back projection in optical projection tomography causes space-variant tangential blurring that increases with the distance to the rotation axis. We present a novel optical tomographic image reconstruction technique that incorporates the point spread function of the imaging lens in an iterative reconstruction. The technique is demonstrated using numerical simulations, tested on experimental optical projection tomography data of single fluorescent beads, and applied to high-resolution emission optical projection tomography imaging of an entire zebrafish larva. Compared to filtered back projection our results show greatly reduced radial and tangential blurring over the entire 5.2×5.2 mm^2 field of view, and a significantly improved signal to noise ratio.

Keywords: image reconstruction techniques, inverse problems, tomographic image processing

S Supplementary material for this article is available online

(Some figures may appear in colour only in the online journal)

1. Introduction

Optical tomographic imaging techniques such as optical diffraction tomography (Wolf 1969) and optical projection tomography (OPT) (Sharpe *et al* 2002) are now among the standard imaging modalities for the study of cells, tissues and small animals. In OPT, light intensity projections of samples, such as zebrafish or (mouse) embryos, are measured in transmission or emission (fluorescence). From these projections, images are computed using tomographic reconstruction algorithms. OPT is used for *in vivo* and *ex vivo* imaging, whereby for *ex vivo* imaging optical clearing techniques are used to suppress light scattering.

In the quest for improved image resolution, high numerical aperture (NA) lenses are used to image the transmission or emission of the sample onto the detector. However, high NA lenses have a small depth of focus (DOF), which causes light that is emitted or absorbed outside of the focal region to be heavily blurred in the detector plane, thereby limiting the imaging depth. Moreover, standard reconstruction techniques, such as filtered back projection (FBP), are generally based on a straight ray approximation and ignore the diffraction of the light by the focusing lens. As a result, reconstructed OPT images can suffer from severe image degradation, leading to tangential blurring that increases with the distance to the rotation axis in the reconstructed image.

Hardware-based approaches to solve the depth of focus effect are either based on off-center focusing (Chen *et al* 2013) or scanning the focal plane through the sample (Miao *et al* 2010). Although, these techniques can reduce the depth of focus effect in the reconstructed image, they are complex to apply and increase the acquisition time.

A sinogram filtering technique using the frequency distance relationship (FDR) was developed by Xia *et al* (1995), in which a space-variant inverse filter is applied to process the sinogram in Fourier space. The physical PSF of an optical imaging system was used as a filter in the FDR reconstruction of OPT data by Walls *et al* (2007). In this method the image is reconstructed, after filtering the sinogram, using standard FBP. A weighted FBP for quantitative fluorescence optical projection tomography was presented by Darrell *et al* (2008). They used a space-variant weighting in the FBP reconstruction to correct for defocus related blur and isotropic emission of the fluorophores. However, this filter was only applied in one direction, which resulted in an increased radial full width at half maximum of the point spread function (PSF). To reduce the effect of the DOF both the radial and tangential direction, various processing methods were developed that include the physical PSF. Deconvolution techniques with a space-variant PSF have been applied to the reconstructed image (Nagy and O'Leary 1997, Temerinac-Ott *et al* 2011, Chen *et al* 2012, van der Horst and Kalkman 2016). However, the quality of this technique depends on the choice of many parameters of the applied reconstruction algorithm. Furthermore, deconvolution techniques have the disadvantage to amplify noise. To our knowledge, the PSF has been used for reconstruction in terahertz and in medical tomographic techniques, such as terahertz tomography (Recur *et al* 2012), PET (Rapisarda *et al* 2010), SPECT (Formiconi *et al* 1989) and CT (Chen and Ning 2004). Recur *et al* (2012) presented an iterative approach, where the object is reconstructed with the straight ray inverse Radon transform and subsequently deconvolved with a Gaussian PSF. For SPECT imaging, the system response was taking into account in an iterative conjugate gradient reconstruction method by Formiconi *et al* (1989). They showed that the inclusion of the PSF gives improved resolution compared to FBP. An iterative 3D edge-deblurring algorithm for cone-beam CT was proposed by Chen and Ning (2004). The PSF was first approximated by a least-squared approach and then used for a three dimensions deconvolution. However, the image size used by both (Formiconi *et al* 1989, Chen and Ning 2004) was significantly smaller than the current image size used for OPT.

We present a PSF-based optical tomographic image reconstruction approach, in which the PSF of the focusing by the lens is directly included in the tomographic reconstruction, instead of filtering the sinogram before or the image after the reconstruction. First, a theoretical framework is provided that describes the PSF-based reconstruction. The application of the theory is demonstrated using numerical simulations of the tomographic imaging process. Second, our algorithm is tested under well-controlled experimental conditions. Finally, the technique is demonstrated on zebrafish larva imaging.

2. Image formation in optical projection tomography

In optical projection tomography (OPT), the goal is to determine the spatial distribution of absorption or emission strength of an object $f(x, y, z)$ from its projections. In emission OPT, the object is assumed to be homogeneously illuminated with light from the excitation source resulting in an excitation rate that is constant over the object f. A small fraction of the excitation light is absorbed and emitted isotropically. Hence, it is assumed that variations in local emission strength are caused by variations in fluorophore concentration only. The emitted radiation is imaged with an imaging system onto the detector, see figure 1(a).

Following (Gu 2000), and assuming a single emitter at location x, y, z, in the object coordinate system, the intensity in the image space coordinate system is $I(s, t, u) = |h(x + Ms, y + Mt, z - M^2u)|^2$, with h^2 the incoherent PSF and M the magnification of the imaging system. Given the geometry in figure 1(a) with the detector fixed at $u = 0$ and since the object can be considered as a sum of incoherent point sources, the measured intensity is a convolution of the object emission distribution with the PSF $|h(x, y, z)|^2$. For an imaging system with $M = -1$ and $u = 0$ the measured intensity on the detector is

$$I(s, t) = \int_{-\infty}^{\infty}\int_{-\infty}^{\infty}\int_{-\infty}^{\infty} f(x - s, y - t, z - u)|h(x, y, z)|^2 \,\mathrm{d}x\,\mathrm{d}y\,\mathrm{d}z|_{u=0}. \tag{1}$$

In the absence of diffraction, the PSF is $|h(x, y, z)|^2 = \delta(x, y)$. Under these circumstances the convolution in equation (1) results in a line integral of the object $f(x, y, z)$, similar to the Radon transform at zero angle along the propagation direction (Radon and Parks 1986). In OPT, diffraction causes the PSF to be non-ideal. The emitted light, originating along a straight path through the object, is (unsharply) imaged by a lens onto the detector. The shape of the 3D PSF can be calculated by Fourier optics, more in particular by Fresnel propagation of the emitted field through the lens onto the detector (Goodmann 1996, Gu 2000).

Following the derivation by van der Horst and Kalkman (2016) we assume an integration on the detector in the t direction over the entire detector plane, which is a good approximation for objects that have optical properties that vary slowly along the y-axis. In this case the measured intensity in equation (1) becomes proportional to the convolution of the object with a 2D cross-section of the 3D PSF. Since the image of a point emitter by a lens results in a complex shaped PSF, we describe it here through an analytical formula. In this way we can quantitatively validate our approach using simulations and compare our results with theory. We model the PSF $|h(x, z)|^2$ as a Gaussian-shaped beam of the wavelength λ and in focus beam waist w_0 (Siegman 1986) as

$$|h(x, z)|^2 = \left| \frac{1}{\sqrt{1 + \left(\frac{z}{z_R}\right)^2}} \exp\left(-\frac{x^2}{w_0^2\left(1 + \left(\frac{z}{z_R}\right)^2\right)} \right) \right|^2, \tag{2}$$

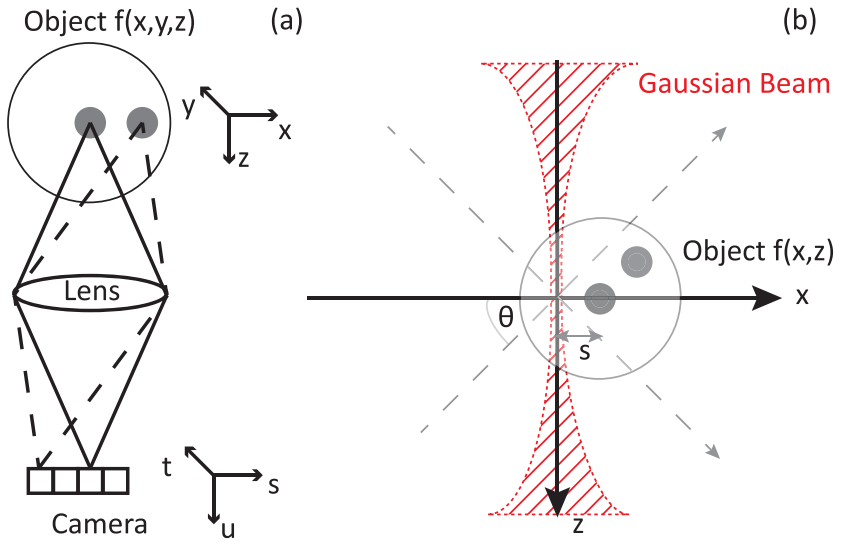

Figure 1. Schematic overview of the optical project tomography imaging system. (a) Optical imaging system consisting of a single lens making a projection of the object onto the camera. (b) OPT signal formation for diffractive optical beams (red dashed and hatched). The rotation angle is denoted by θ, the shift of the object s, and $f(x, z)$ is a slice of the object.

where $z_R = \pi w_0^2/\lambda$ is the Rayleigh range (half the depth of focus). The numerical aperture is given by NA $= w_0/z_R$ in equation (1). The two-dimensional convolution of the PSF over the object is indicated in figure 1(b).

In tomographic imaging, we obtain the projections of the emission as a function of the lateral shift s and the rotation angle θ of the object. From equation (1), it can be derived that the measured projection at the angle θ and shift s is

$$p(s,\theta) = \int_{-\infty}^{\infty} \int f[(x-s)\cos\theta + z\sin\theta, (x-s)\sin\theta - z\cos\theta]\ |h(x,z)|^2\, \mathrm{d}x\, \mathrm{d}z\,, \tag{3}$$

with the angle $\theta \in [0, 2\pi]$. The projections $p(s, \theta)$ are commonly visualized in a sinogram, where the convolution in equation (3) describes the blurring in the sinogram due to the tomographic imaging system.

The projection data $p(s, \theta)$ is not measured in a continuous way, as defined by equation (3), but is sampled at discrete lateral positions for a finite set of angles. Hence, the inverse solution cannot be determined analytically, but only through a search for the function $f(x, z)$ that optimizes an objective function. The projection of equation (3), $p(s, \theta)$, is limited to a finite integration area D given by $D \in [-l/2, l/2]$ for offsets $s \in [-l/2, l/2]$ and l is the size of the field of view. The projection is then represented by a matrix multiplication with the object f discretized by sampling $f(x, z)$ on a regular cell-centered grid, within the square object domain D^2 at locations x_i, z_j, with $i = 1, 2, \ldots, n$, $j = 1, 2, \ldots, n$ where n is the number of pixels in each direction of the object and equal to the number of lateral pixels in the projection. This leads to an image matrix of $f(x_i, z_i) \in \mathbb{R}^{n\times n}$, which is stacked in a vector $\mathbf{f} \in \mathbb{R}^{n^2}$. The convolution of equation (3) is discretized into a geometry matrix $\mathbf{A} \in \mathbb{R}^{m\cdot n, n^2}$, with m the

number of projection angles. A row of the matrix **A** represents a the Gaussian PSF at lateral distance s_i and angle θ_k. The matrix elements of **A** are

$$a_{(k-1)n+i,:} = |h[(x_i - s_i)\cos\theta_k + z_i \sin\theta_k, (x_i - s_i)\sin\theta_k - z_i \cos\theta_k]|^2. \quad (4)$$

In this way, a shifted and rotated PSF is represented in a single row of the **A** matrix. First, all shifts for one angle are addressed, which is subsequently repeated for all angles. The acquisition domain of the measured projections are the set of samples (s_i, θ_k), with $k = 1, 2, \ldots, m$. The discrete projections $p(s_i, \theta_k) \in \mathbb{R}^{n,m}$ are stacked into a vector $\mathbf{p} \in \mathbb{R}^{n\cdot m,1}$.

After discretization, the object, **f**, can be reconstructed by finding a solution to the optimization problem

$$\underset{\mathbf{f}}{\text{argmin}} \quad \frac{1}{2}\|\mathbf{A}\cdot\mathbf{f} - \mathbf{p}\|_2^2, \quad (5)$$

where $\|\cdot\|_2$ denotes the Euclidean norm. Equation (5) can be solved using a least squares optimization method based on conjugate gradients.

3. Image reconstruction

Tomographic reconstructions are performed on a computer with Intel(R) Xeon(R) CPU Processor (E5-1620 v3@3.50 GHz), 32 GB installed memory and a 64-bit operating system. The data are processed using software written in the commercial software package MATLAB (Mathworks, R2016a). Simulated sinograms are constructed using the discretized version of equation (3) for an initial object *f*. Following the data processing flow chart in figure 2, an initial guess of the image is created by filtered back projection (FBP) (input reconstruction). An improved estimate for the object is made by least-squares optimization of equation (5) using the MATLAB function *lsqr* (Paige and Saunders 1982, Barrett *et al* 1994), which uses a conjugate-gradient type iterative algorithm on the normal equations. It takes as input the projection data, the initial guess of the image (created by FBP), the maximum number of iterations to perform set to 4000, the absolute tolerance, and the geometry matrix **A**. The absolute tolerance of the method is chosen to be 10^{-6}. If the algorithm stops at the maximum number of iterations before the absolute tolerance is reached, the reconstruction results are evaluated by visual inspection. The PSF-based reconstruction is performed without including any prior information or regularization in the optimization of equation (5).

The geometry matrix **A** is non-sparse and therefore explicitly computing and storing it for a realistic image size of 1000 by 1000 would require around 8 terabytes of memory, which is infeasible. Instead of requiring a precomputed version of **A**, the MATLAB function *lsqr* also allows providing a routine that evaluates multiplication by **A** and its transpose for every angle individually. Here, multiplication by **A** corresponds to (PSF-based) forward projection of an input image, and multiplication by the transpose of **A** corresponds to (PSF-based) back projection of an input sinogram. We list the pseudo-code for calculating the forward and backward projection in algorithm 1. It uses the built-in MATLAB function *imrotate* with bilinear interpolation to obtain the object at different angles. For every individual angle, the PSF is translated laterally over the sample, so the forward model of the projection has the structure of a one-dimensional convolution in the translation direction, followed by a sum in the direction orthogonal to that. We implement this by a multiplication of the Fourier transform of the object and the Fourier transform of the PSF for every column, followed by a sum for every

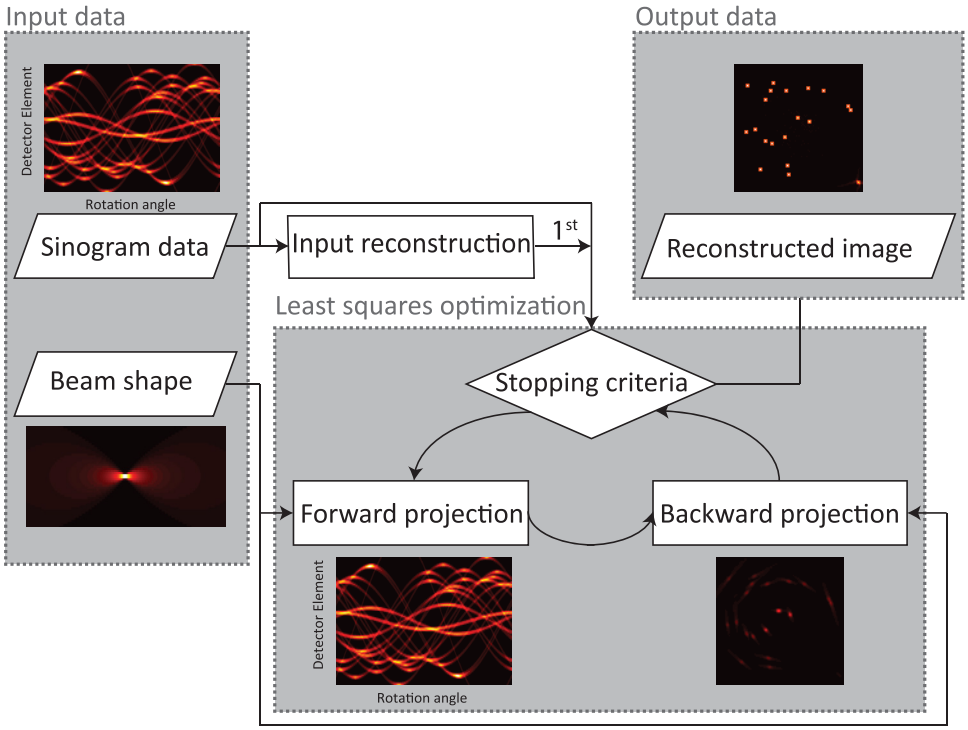

Figure 2. Schematic illustration of the data analysis algorithm for the PSF-based reconstruction. The input reconstruction is only used in the first iteration.

row. To perform these operation correctly we zero-pad the sinogram to twice its size in the scanning direction. The back projection operator performs the adjoint/transpose variants of these steps in reverse order.

We set the maximum number of *lsqr* iterations to different hand-picked numbers depending on the convergence of the algorithm, which depends on the data that is to be reconstructed. In the current implementation one iteration of the *lsqr* algorithm, for one slice of 1000 by 1000 pixels, takes approximately two minutes.

To enable a qualitative comparison of the reconstructed images, the FBP reconstruction is scaled in the following way. The reconstructed FBP image is forward projected to obtain its sinogram. The scaling factor α_{opt} is then given by

$$\alpha_{\text{opt}} = \underset{\alpha}{\text{argmin}} \quad \|\alpha \mathbf{A}\mathbf{f}_1 - \mathbf{A}\mathbf{f}_2\|_2^2, \tag{6}$$

where $\mathbf{f_1}$ is the FBP reconstructed image and $\mathbf{f_2}$ the PSF-based reconstructed image. The scaling factor α_{opt} is then given in closed-form by

$$\alpha_{\text{opt}} = \frac{(\mathbf{A}\mathbf{f}_1)^{\text{T}}(\mathbf{A}\mathbf{f}_2)}{\|\mathbf{A}\mathbf{f}_1\|_2^2}. \tag{7}$$

Subsequently, the FBP reconstruction is scaled with α_{opt} to obtain an image intensity distribution in the reconstruction that corresponds to equal projection data[4].

[4] Our code to perform these calculations can be made available on request.

Algorithm 1 . Calculate $\mathbf{p} = \mathbf{Af}$ or $\mathbf{f} = \mathbf{A}^{\mathrm{T}}\mathbf{p}$

Require: $\mathbf{f}$, *mode*, beam parameters
Notation: Denote by $(\mathrm{I})\mathrm{FT}_{\mathrm{C}}$ taking an (inverse) 1D Fourier transform of every column of an image, by $(\mathrm{I})\mathrm{FT}_{1}$ taking the (inverse) 1D Fourier transform, by $\mathrm{Sum}_{\mathrm{R}}$ taking the sum of every row of an image, and by $\mathbf{p}^{i}$ the ith row of a sinogram $\mathbf{p}$.
Pre-compute the 2D beam shape of a horizontal beam and $\mathrm{FT}_{\mathrm{C}}(\mathrm{Beam})$
if mode = 'not transposed', **then** ▷ Forward operator, $\mathbf{p} = \mathbf{Af}$
  for $i = 1 : \mathrm{angle}_{\mathrm{count}}$ **do**
    $\mathbf{f}_r = \mathbf{f}$ rotated by the current angle
    $\mathbf{p}^{i} = \mathrm{IFT}_{1}(\mathrm{Sum}_{\mathrm{R}}(\mathrm{FT}_{\mathrm{C}}(\mathbf{f}_{\mathrm{r}}) \cdot \mathrm{FT}_{\mathrm{C}}(\mathrm{Beam})))$
else ▷ Backward operator, $\mathbf{f} = \mathbf{A}^{\mathrm{T}}\mathbf{p}$
  $\mathbf{f}$ = the zero image
  for $i = 1 : \mathrm{angle}_{\mathrm{count}}$ **do**
    $\mathbf{t}$ = Multiply each column of $\mathrm{FT}_{\mathrm{C}}(\mathrm{Beam})$ by $\mathrm{FT}_{1}(\mathbf{p}^{i})$
    $\mathbf{u} = \mathrm{IFT}_{\mathrm{C}}(t)$ rotated by the reverse angle
    $\mathbf{f} = \mathbf{f} + \mathbf{u}$
return $\mathbf{p}$ or $\mathbf{f}$

4. Results

4.1. OPT simulations

The original object for the simulation is given in figure 3(a). The object, with a size of 15×15 mm^2 (100×100 pixels), consists of isolated point sources, with a peak emission strength of 100 in the center pixel of the source and an emission strength set to 50 for the eight pixels around the center of the source. The object is blurred by convolving it with a Gaussian PSF for an emission wavelength of 514 nm with a waist $w_0 = 10$ μm, DOF= 1.2 mm, NA= 0.016, see figure 3(b). Figure 3(c) shows the same simulation for $w_0 = 100$ μm, DOF = 122 mm, NA= 0.0016. The object data is processed following the flowchart in figure 2. The maximum number of iterations is set to 200.

The reconstruction results using filtered back projection (MATLAB function *iradon*) and the proposed method are depicted in figure 3. Figures 3(d) and (e) show the FBP reconstructed images, which is based on straight parallel rays, for the two Gaussian PSFs. In figure 3(d) it is clearly visible that, compared to the original object, the emission contrast is much lower due to the small DOF. Moreover, the reconstructed image shows that the emitters are strongly blurred in the tangential direction due to the strong divergence of the Gaussian PSF, as shown in figure 3(b). The tangential resolution deteriorates with increasing distance to the center of rotation whereas the radial resolution is slightly deteriorated, but does not depend on the distance from the center of rotation. The insets show this in more detail for two emitters. For a PSF with a larger beam waist, modeling a low NA, large DOF, imaging system, figure 3(e) shows that there is some blurring in the reconstructed image. However, for this larger beam waist this effect depend very weakly on the distance to the center of rotation since the Gaussian PSF has much lower divergence, as shown in figure 3(c). Figures 3(f) and (g) show our PSF-based reconstruction. In figure 3(f) the contrast is completely restored, the strong tangential blurring is absent, and the reconstructed image is identical to the input image. Figure 3(g) shows that

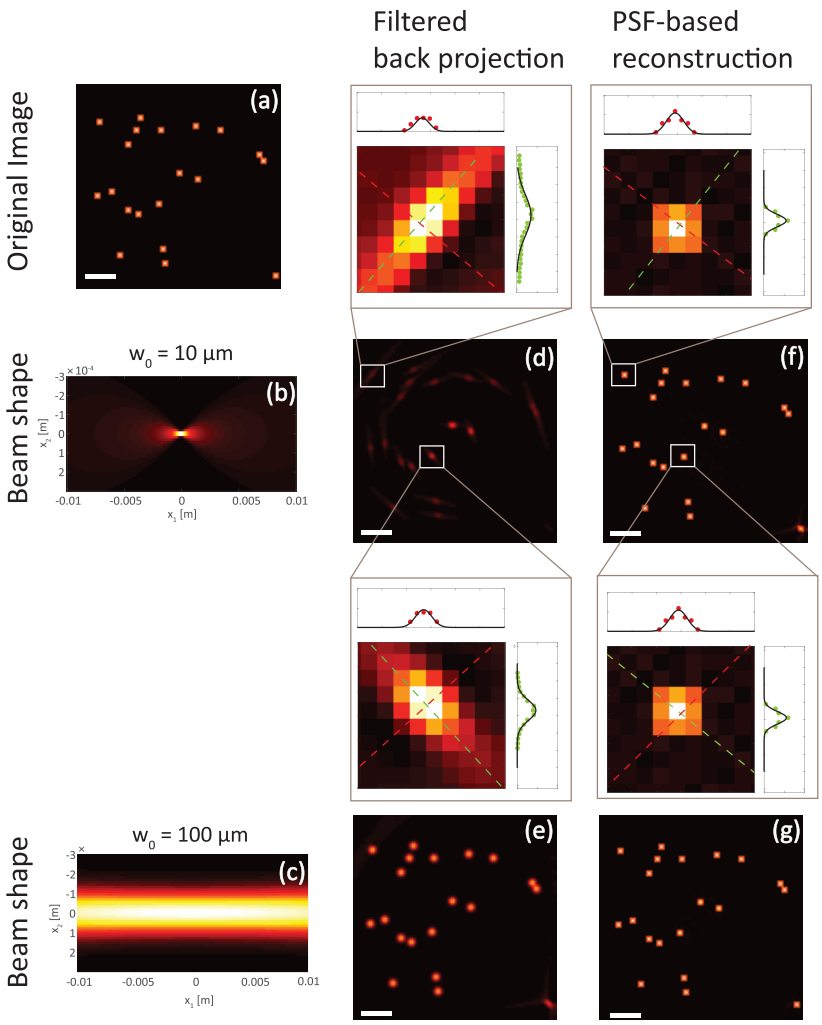

Figure 3. Simulation of the FBP and PSF-based image reconstruction. (a) Input image, (b) Gaussian PSF for $w_0 = 10$ μm. (c) Gaussian PSF for $w_0 = 100$ μm. ((d) and (e)) Reconstruction using FBP for the two Gaussian PSFs. ((f) and (g)) Reconstruction using the PSF-based approach for the two Gaussian PSFs. The scale bar is 2.5 mm.

also for a larger beam waist, the blurring of the emitter is fully corrected for by our PSF-based reconstruction method.

4.2. Fluorescent bead OPT imaging

The PSF-based reconstruction method is tested with experimental OPT imaging of a sample with fluorescent bead emitters embedded in an agarose emulsion. The experimental set-up is described in more detail in van der Horst and Kalkman (2016), the main parameters of importance are briefly discussed. The experimentally determined Gaussian PSF has a beam waist in focus of $w_0 = 6$ μm with the measured beam shape used in the PSF-based reconstruction. Emission from the center of the object is focused onto the camera plane by the imaging lens. The field of view of the experimental data is 5.2×5.2 mm^2. In the lateral direction, the

detector has 1344 pixels per projection and 360 projections are acquired over 360 degrees with a one degree spacing. The total dataset consist of 1024 sinograms covering a length of 4 mm along the rotation axis. The NA of the system is 0.05.

The measured data is pre-processed as follows. First, photo bleaching is corrected with a characteristic e^{-1} timescale of 798 seconds. Second, a constant background emission is removed from the sinogram. Third, the center of mass for each projection is estimated from the ratio of the integral of the projection times its transverse coordinate to the integral of the projection. Fourth, the center of rotation is determined from the centers of mass for all acquisition angles. Fifth, the center of rotation of the object is aligned with the center of the detector rows by shifting the data along the lateral dimension (Azevedo *et al* 1990). Subsequently, the 1024 sinograms are combined into 32 averaged sinograms. The averaged sinograms are further pre-processed. The noise is reduced by applying a non-local means de-noising algorithm as described by Buades *et al* (2004). The half size for the de-noising window is chosen to be 9 pixels. The width of the Gaussian filter relative to its maximum intensity is set to 0.5, the search width is set to 10 pixels and the limited number of dimensions for the principal component analysis is 20. Prior to the reconstruction, the FBP sinogram is scaled to achieve a quantitative comparison of the image quality of the two methods. Subsequently, PSF-based reconstruction of the data is performed up to the maximum number of 4000 iterations and visually inspection confirmed the convergence.

Figure 4(a) shows the reconstruction of an averaged sinogram of the experimental data using FBP. Similar to the simulations, the single point emitters appear blurred in the FBP reconstruction. In figure 4(b) this is more clearly demonstrated by the zoom-in on the individual beads and the normalized cross-sections of the emitters. The cross sections show that the emission profiles in the reconstruction are broad and have a Gaussian-shape. Figure 4(c) shows the same emitters, but reconstructed with our PSF-based approach. The emitters are brighter in comparison to the background and an improvement of the resolution is visible compared to the reconstruction using FBP. The quality of the reconstruction is analyzed by estimating the full width at half maximum (FWHM) of the Gaussian function fitted to each peak and is summarized table 1. Our PSF-based reconstruction shows a significant reduction of the FWHM in both axial and tangential direction. Figure 4(d) shows the same slide as in figure 4(a) reconstructed with the PSF-based reconstruction. The side lobes of the single bead 1 are 'Gibbs' like artefacts (Rapisarda *et al* 2010). The relative large distant to the center of rotation makes it difficult to correctly reconstruct the image of this bead.

4.3. Zebrafish larva OPT imaging

The proposed PSF-based reconstruction is applied to an OPT scan of a 10 d old transgenic zebrafish larva to illustrate the performance on biological samples. The zebrafish cellular membranes are labeled with green fluorescent protein. The zebrafish larva is euthanized in ice water at the Erasmus Medical Center, Rotterdam according to animal welfare regulations. Animal experiments are approved by the Animal Experimentation Committee of the Erasmus MC, Rotterdam.

The zebrafish is mounted in agarose in our OPT system. The same experimental parameters are used as for the fluorescent bead data, but for the zebrafish imaging a total of 1791 sinograms are acquired covering a distance of 6.9 mm along the rotation axis. The NA of the system is 0.02. For all 1791 slices, the tomographic image is reconstructed using FBP and the PSF-based approach (no slice averaging). Prior to the reconstruction, the sinograms are scaled to achieve a better quantitative comparison of the two methods. The number of

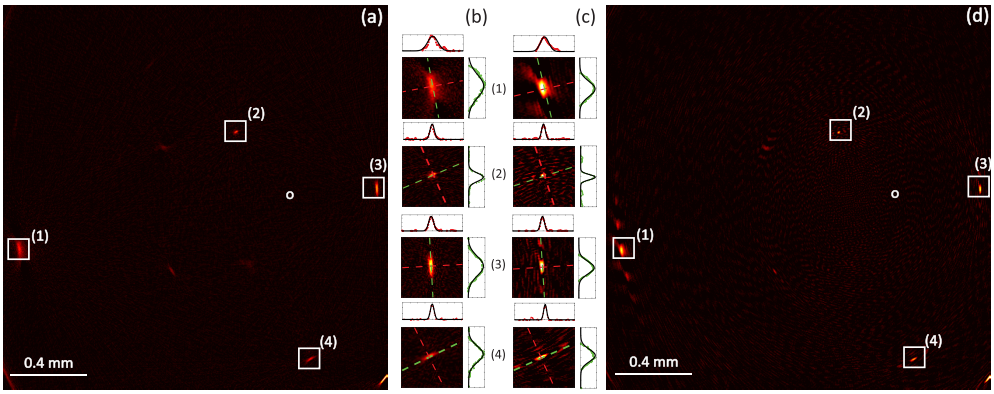

Figure 4. Comparison of the FBP and PSF-based reconstruction for a single averaged sinogram. (a) FBP image reconstruction of fluorescent bead data. The circle denotes the center of rotation. (b) Zoom in on reconstructed points of (a). (c) PSF-based reconstruction of the same points as in (b). (d) PSF-based reconstruction.

Table 1. FWHM resolution (μm) in axial and tangential direction for the FBP and the PSF-based reconstruction for four fluorescent beads. Each row corresponds to the beads indicated in figure 4. The errors indicate 95 % confidence intervals.

	FBP		PSF-based	
Method Bead #	Radial FWHM	Tangential FWHM	Radial FWHM	Tangential FWHM
1	22.3 ± 0.6	50.1 ± 1.3	16.2 ± 0.6	30.0 ± 1.0
2	9.6 ± 0.3	18.0 ± 0.5	7.1 ± 0.3	10.0 ± 0.4
3	10.7 ± 0.13	42.1 ± 0.6	8.3 ± 0.2	24.9 ± 0.5
4	8.3 ± 0.2	34.9 ± 0.9	6.3 ± 0.2	24.0 ± 0.6

iterations is evaluated for one slide and is set to two, for which good convergence of the reconstruction is visually observed. Afterward this number of iterations is applied to the whole dataset. The reconstruction of the zebrafish larva is depicted in figure 5. Figure 5(a) shows the reconstruction of a single transverse slice of the data using FBP. Although the zebrafish structure is visible, the reconstruction is corrupted by radial streak artifacts, shows significant blurring, and has limited image contrast. Figure 5(b) shows our PSF-based reconstruction of the same transverse slice. Figure 5(c) shows the anatomy of an optical cleared zebrafish larva, of similar age, in transverse view obtained from transmission OPT from the zebrafish anatomy portal (Salgadob *et al* 2012) and is used for anatomical reference. The quality of the reconstructed image is significantly improved in terms of contrast, artifact removal, and resolution. Figures 5(d) and (e) show two cross sections through the data that illustrate the large improvement in image contrast and resolution. In our PSF-based reconstructed image the major anatomical parts are much better resolved compared to the reconstruction using FBP (see figures 5(a) and (b)). Similar effects are visible in figure 6, which shows a coronal cross-section through the same data. Figures 6(a) and (b) show the reconstruction using FBP and the PSF-based reconstruction. Figure 6(c) shows a transmission OPT image of the anatomy of a 7–13 d old, optically cleared, zebrafish larva in coronal view (Salgadob *et al* 2012). An even better view on the obtained image improvement achieved by our PSF-based reconstruction can be seen in a video (visualization 1) (stacks.iop.org/PMB/62/7784/mmedia), which shows

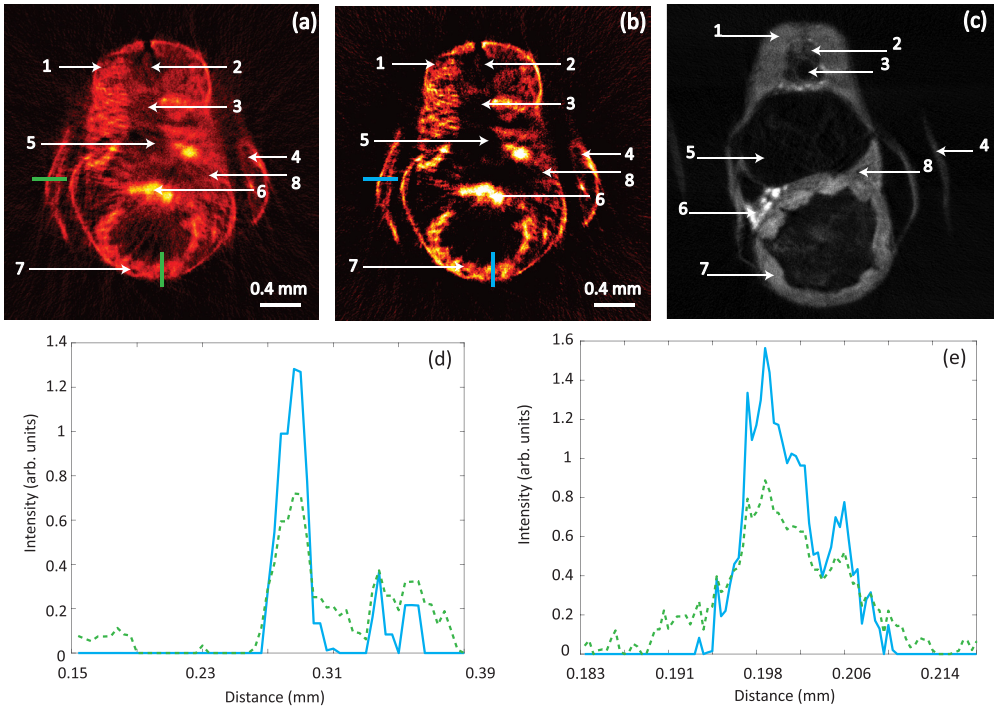

Figure 5. Transversal slice through the OPT reconstruction of a zebrafish larva. (a) FBP reconstruction with anatomical structures indicated. (b) PSF-based reconstruction. (c) Anatomy of a 7–13 d old optical cleared zebrafish larva (Salgadob *et al* 2012), with anatomical features: (1) myotome, (2) spinal cord, (3) precaudal vertebra, (4) pectoral fin, (5) anterior chamber swim bladder, (6) pancreas, (7) intestinal bulb and (8) liver. (d) Cross-section in horizontal direction at line indicated in ((a) and (b)). (e) Cross-section in vertical direction at line indicated in ((a) and (b)). In ((d) and (e)) the green dashed line indicates the FBP and the blue solid line indicates the PSF-based approach.

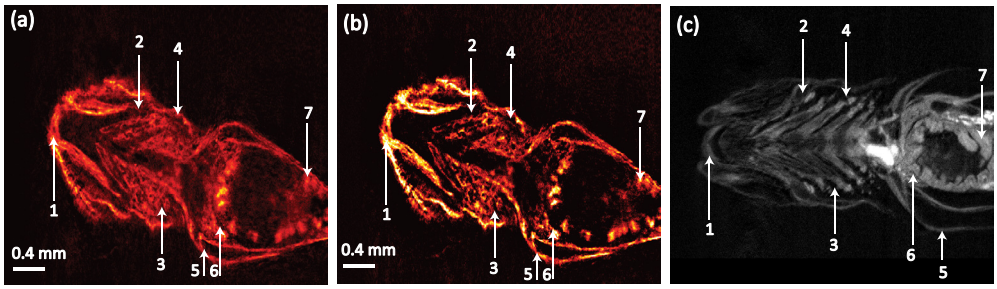

Figure 6. Coronal slice through the OPT reconstruction of a zebrafish larva (excluding the tail). (a) FBP reconstruction with anatomical structures indicated. (b) PSF-based reconstruction. (c) Anatomy of a 7–13 d old optical cleared zebrafish larva (Salgadob *et al* 2012), with anatomical features: (1) intermandibularis, (2) ceratohyal, (3) opercular cavity, (4) opercle, (5) pectorial fin, (6) liver and (7) intestinal bulb.

a side by side comparison of transverse, coronal, and sagittal planes of the zebrafish using both reconstruction techniques.

5. Discussion and conclusion

We present a tomographic image reconstruction algorithm, where the physical PSF is included in the reconstruction. Our PSF-based image reconstruction approach shows a significant improvement in OPT image quality compared to standard FBP reconstruction. In contrast to other approaches, our method incorporates the imaging geometry in the tomographic image reconstruction. As such we do not rely on filtering or deconvolution methods applied in the sinogram or image domain. A quantitative comparison of the quality of our image reconstruction algorithm with other state-of-the-art image reconstruction techniques is currently in progress (Trull 2017). The presented reconstruction method employs a 2D reconstruction, processing the data volume slice by slice. Despite this simplification, excellent image quality is obtained. We attribute this to the fact that the zebrafish has structures that, in general, vary slowly along the length of the zebrafish. In principle our PSF-based approach could be extended to three dimensions, however, this would significantly increase the memory requirements of the routine that performs the multiplication with the system matrix and its transpose, as well as the computation time. For the full image size of 1344 by 1024 pixels, this 3D implementation is currently not feasible.

The reconstruction time for one slice using the PSF-based algorithm is currently about two minutes for one iteration. This potentially can be reduced by converting the presented algorithm from MATLAB to another programming language, such as C++, or using a GPU. Moreover, for a slice-based reconstruction of three-dimensional objects, the reconstruction of different slices can be parallelized. A speed-up by a factor of 200 has been observed by Leeser *et al* for parallel slice processing in CT reconstruction (Leeser *et al* 2014). Finally, since the PSF is varying slowly over many of the grid-points, relatively few grid points sample the beam at its narrow waist in the focal area. Hence, by representing the reconstruction problem in a different set of basis functions, potentially the size of the reconstruction problem can be reduced while obtaining the same reconstruction result.

In the reconstructions we observed that the convergence of the algorithm is strongly related to the noise level in the projections. The presented fluorophore bead data had an SNR, averaged over all the sinograms, of 31 ± 3 dB, whereas the zebrafish data had an average SNR of 67 ± 10 dB. Moreover, the zebrafish data is non-sparse compared to the bead data, which promotes convergence. As a result, the reconstruction of the fluorophore beads needed 4000 iterations, whereas the reconstruction of the zebrafish needed only 2 iterations to convergence.

In its current implementation, the PSF-based reconstruction is without including any prior information or regularization. Improvement of the convergence of the optimization possibly can be achieved by masking the data or by applying regularization methods. For example, for the sparse bead sample reconstruction, sparsity promoting ℓ_1 norm regularization, can aid in the reconstruction accuracy as well as in the convergence rate as was shown by Kim *et al* (2007).

The proposed reconstruction technique can be extended to even higher NAs, potentially further improving the image resolution. Besides the significantly improved image quality, our PSF-based reconstruction has the advantage that arbitrary beam shapes can be incorporated in the reconstruction. In addition, other physical processes, such as refraction or scattering, can be included in the PSF-based reconstruction (Haidekker 2005). The presented PSF-based reconstruction is useful in other fields of optical tomographic imaging where beam propagation

deviates from the ideal straight ray such as in optical diffraction tomography, transmission OPT, electron tomography, terahertz tomography, and (phase-contrast) x-ray tomography.

Acknowledgments

The authors would like to thank Dr Robert Bryson-Richardson of the School of Biological Sciences, Monash University, Australia for the use of the transmission OPT images. This research is supported by the Dutch Technology Foundation Toegepaste en Technische Wetenschappen, which is part of the Netherlands Organization for Scientific Research, and which is partly funded by the Ministry of Economic Affairs.

ORCID iDs

Willem Jan Palenstijn https://orcid.org/0000-0003-0511-4763
Jeroen Kalkman https://orcid.org/0000-0003-1698-7842

References

Azevedo S G, Schneberk D F, Fitch J P and Martz H E 1990 Calculation of the rotational centers in computed tomography sinogram *IEEE Trans. Nucl. Sci.* **37** 1525–40
Barrett R, Berry M, Chan T F, Demmel J, Donato J, Dongarra J, Eijkhout V, Pozo R, Romine C and der Vors H V 1994 Templates for the solution of linear systems: building blocks for iterative methods *SIAM* (https://doi.org/10.1137/1.9781611971538)
Buades A, Coll B and Morel J M 2004 On image denoising methods *Technical Report* CMLA (Centre de Mathematiques et de Leurs Applications)
Chen L, Andrews N, Kumar S, Frankel P, McGinty J and French P M 2013 Simultaneous angular multiplexing optical projection tomography at shifted focal planes *Opt. Lett.* **38** 851–3
Chen L, McGinty J, Taylor H B, Bugeon L, Lamb J R, Dallman M J and French P M W 2012 Incorporation of an experimentally determined MTF for spatial frequency filtering and deconvolution during optical projection tomography reconstruction *Opt. Express* **20** 7323–37
Chen Z and Ning R 2004 Three-dimensional point spread function measurement of cone-beam computed tomography system by iterative edge-blurring algorithm *Phys. Med. Biol.* **49** 1865–80
Darrell A, Meyer H, Marias K, Brady M and Ripoll J 2008 Weighted filtered backprojection for quantitative fluorescence optical projection tomography *Phys. Med. Biol.* **53** 38633881
Formiconi R, Pupi A and Passeri A 1989 Compensation of spatial system response in SPECT with conjugate gradient reconstruction technique *Phys. Med. Biol.* **34** 68–84
Goodmann J 1996 *Introduction to Fourier Optics* 2nd edn (New York: MaGraw-Hill)
Gu M 2000 *Advanced Optical Imaging Theory* (Berlin: Springer)
Haidekker M 2005 Optical transillumination tomography with tolerance against refraction mismatch *Comput. Methods Programs Biomed.* **3** 225–35
Kim S J, Koh K, Lustig M, Boyd S and Gorinevsky D 2007 An interior-point method for large-scale l_1-regularized least squares *IEEE J. Sel. Top. Signal Process.* **1** 606–17
Leeser M, Mukherjee S and Brock J 2014 Fast reconstruction of 3D volumes from 2D CT projection data with GPUs *BMC Res. Notes* (https://doi.org/10.1186/1756-0500-7-582)
Miao Q, Hayenga J, Meyer M G, Neumann T, Nelson A C and Seibel E J 2010 Resolution improvement in optical projection tomography by the focal scanning method *Opt. Lett.* **35** 3363–5
Nagy J G and O'Leary D P 1997 Fast iterative image restoration with a spatially-varying PSF *Proc. SPIE 3162, Adv. Signal Process.* **3162** 884
Paige C C and Saunders M A 1982 LSQR: an algorithm for sparse linear equations and sparse least squares *ACM* **8** 43–71
Radon J and Parks P 1986 On the determination of functions from their integral values along certain manifolds *IEEE Trans. Med. Imaging* **4** 170176

Rapisarda E, Bettinardi V, Thielemans K and Gilardi M C 2010 Image-based point spread function implementation in a fully 3d OSEM reconstruction algorithm for PET *Phys. Med. Biol.* **34** 4131–51

Recur B, Guillet J P, Manek-Hönninger I, Delagnes J C, Benharbone W, Desbarats P, Domenger J P, Canioni L and Mounaix P 2012 Propagation beam consideration for 3D THz computed tomography *Opt. Express* **20** 5817–29

Salgadob D, Marcelleb C, Currieb P D and Bryson-Richardson R J 2012 The zebrafish anatomy portal a novel integrated resource to facilitate zebrafish research *Dev. Bio.* **372** 1–4

Sharpe J, Ahlgren U, Perry P, Hill B, Ross A, Hecksher-Sørensen J, Baldock R and Davidson D 2002 Optical projection tomography as a tool for 3D microscopy and gene expression studies *Science* **296** 541–5

Siegman A E 1986 *Lasers* (Sausalito, CA: University Science Books)

Temerinac-Ott M, Ronneberger O, Nitschke R, Driever W and Burkhardt H 2011 Spatially variant Lucy Richardson deconvolution for multiview fusion of microscopal 3D images *IEEE Int. Symp. Biomed. Imaging* pp 899–904

Trull A 2017 Comparison of image reconstruction techniques in optical projection tomography, manuscript in preparation

van der Horst J and Kalkman J 2016 Image resolution and deconvolution in optical tomography *Opt. Express* **24** 24460–72

Walls J R, Sled J G and Sharp J 2007 Resolution improvement in emission optical projection tomography *Phys. Med. Biol.* **52** 2775–90

Wolf E 1969 Three-dimensional structure determination of semi-transparent objects from holographic data *Opt. Commun.* **1** 153–6

Xia W, Lewitt R M and Edholm P R 1995 Fourier correction for spatially variant collimator blurring in SPECT *IEEE Trans. Med. Imaging* **14** 100–15